Journal of Materials Chemistry A

ROYAL SOCIETY OF CHEMISTRY

PAPER

View Article Online
View Journal

Cite this: DOI: 10.1039/d5ta10289h

Engineering hydrolytic stability and reversible O3/P3/OP2 transitions in O3-type sodium-ion battery cathodes through Cu^{2+} doping

Sang Hyuk Gong,[a] Hyeongwoo Kim,[a] Min Kyung Cho,[b] Hyojun Lim,[a] Hyun Beom Kang,[ac] Jae-Ho Park,[a] Sung-Chul Kim,[b] Elang Barruna,[ad] Kyung Yoon Chung,[ad] Wonyoung Chang,[ad] Wonchang Choi *[e] and Hyung-Seok Kim *[adf]

O3-type layered oxides have emerged as promising cathode materials for sodium-ion batteries (SIBs) owing to their competitive energy density and structural robustness. However, their inherent sensitivity to moisture remains a critical obstacle for practical application. In this study, we introduced Cu^{2+} doping into $NaNi_{0.3}Fe_{0.2}Mn_{0.5}O_2$ (NFM325) to synthesize $NaNi_{0.3}Fe_{0.2}Cu_{0.1}Mn_{0.4}O_2$ (NFCM3214). Comprehensive analyses (XRD, FTIR, TGA, XPS, SEM, and TEM) demonstrate that Cu incorporation prevents bulk degradation and suppresses surface reactions such as Na^+/H^+ exchange and the formation of NaOH and Mn hydroxides upon water exposure. These local structural modifications enhance both bulk and surface stability against moisture. Electrochemical evaluations confirm that NFCM3214 retains 89% of its initial capacity after direct water contact, with significantly improved Na^+ diffusivity, rate capability (7.2 → 88.8 mAh g^{-1} at 700 mA g^{-1}), and cycling retention (71.4% → 84.5% after 100 cycles). Mechanistic insights further reveal that Cu^{2+} doping mitigates Jahn–Teller distortion, promotes the formation of an OP2 intermediate phase during deep desodiation, and facilitates reversible OP2–O/P transitions during cycling. Finally, full-cell tests using an N-doped MoS_2 anode demonstrate high capacity and stable cycling performance, underscoring the practical potential of Cu-doped O3-type layered oxides for advanced sodium-ion batteries.

Received 17th December 2025
Accepted 31st March 2026

DOI: 10.1039/d5ta10289h

rsc.li/materials-a

1. Introduction

Recently, there has been a problem with the supply and demand of lithium materials required to produce lithium-ion batteries for medium- and large-scale energy storage devices. In particular, the demand for lithium sources has increased rapidly due to the widespread use of electric vehicles. Therefore, the price of lithium sources for batteries continues to increase. In this sense, abundant sodium sources from the sea have made sodium-ion batteries (SIBs) a more suitable battery system for large-scale energy storage systems than lithium-ion batteries (LIBs).[1] In addition, SIBs have charge/discharge mechanisms similar to lithium-ion batteries; therefore, a number of parts currently employed in the cell composition can be used as they are. Furthermore, the current lithium-ion battery manufacturing platform can be used as well, which is expected to be advantageous for commercialization and mass production.[2] From the perspective of high-energy cathode materials for SIBs, numerous research groups have regarded layered oxide structures (Na_xTMO_2, where TM = Ni, Fe, Mn, Co, Ti, Cr, *etc.*, and their combinations) as promising candidates.[3–10] Generally, there are two major stacking modes of MO_6 octahedra in sodium-layered oxides, which can be classified as P2 or O3. The P2 structure exhibits an ABBA stacking mode with a prismatic Na^+ site, whereas the O3 structure exhibits ABCABC stacking with an octahedral Na^+ site.[11]

O3-type layered oxides have more advantages in terms of higher initial capacity and coulombic efficiency than P2-type structures.[12] There have been numerous reports on binary or ternary O3-type cathode materials for SIBs comparable to layered oxide cathodes (*e.g.*, $LiCoO_2$) in LIBs.[13–15] Primarily, Co-free and Ni- and Mn-based layered oxides are considered suitable configurations for high-energy and low-cost SIBs, offering advantages in resource sustainability and supply-chain stability

[a]Energy Storage Research Center, Korea Institute of Science and Technology, Seoul 02792, Republic of Korea. E-mail: hskim0227@kist.re.kr
[b]Advanced Analysis Center, Korea Institute of Science and Technology, Seoul 02792, Republic of Korea
[c]Department of Materials Science and Engineering, Korea University, Seoul 02841, Republic of Korea
[d]Division of Energy & Environment Technology, KIST School, Korea University of Science and Technology, Seoul 02792, Republic of Korea
[e]Department of Energy Engineering, Konkuk University, Seoul 05029, Republic of Korea. E-mail: wcchoi@konkuk.ac.kr
[f]Yonsei-KIST Convergence Research Institute, Yonsei University, Seoul 03722, Republic of Korea

that are crucial for large-scale industrial deployment.[16] For instance, Komaba *et al.* reported that O3-type $NaNi_{0.5}Mn_{0.5}O_2$ shows a high capacity of ~185 mAh g^{-1}.[8] However, multiple phase transitions (O3–O′3–P3–P′3–P3″) during the Na^+ extraction process trigger irreversible capacity loss with structural instability. In addition to Ni and Mn, inexpensive and electrochemically active iron is attracting attention as an element for the ternary O3-type cathode. Appropriate Fe addition to Ni–Mn-based oxides can increase the cyclability and capacity (*e.g.*, $NaFe_x(Ni_{0.5}Mn_{0.5})_{1-x}O_2$ and $NaNi_{1/3}Fe_{1/3}Mn_{1/3}O_2$).[17] Furthermore, Sb^{5+} or La^{3+} doping strategies have also been explored to regulate the local crystal environment of Ni–Mn-based oxides, thereby lowering the Na^+ migration barrier and enhancing ionic diffusion kinetics.[18,19] Despite these efforts, the irreversible phase transition of ternary O3-type layered oxides during high-voltage operation remains a major hurdle in increasing the energy density of electrochemical cells. Therefore, doping strategies with electrochemically inactive foreign elements, such as Ti,[20] Zr,[21] Zn,[22] and Ca,[23] have been considered to ensure high-voltage stability of the cathode material. Doping these elements into the layered structure effectively suppressed the formation of large interslab distances at the end of the charge, thereby enhancing the structural stability.

However, O3-type layered oxides have not only these structural instabilities during charge/discharge but also poor air and moisture stability, resulting in severe capacity decay.[24] The poor air/moisture stability is a crucial problem in the practical application of O3-type materials. This is because poor air/moisture stability can increase the cost of material storage, transportation, and battery manufacturing, thereby limiting its practical application. Researchers have investigated the root cause of this issue, finding that exposure to air, particularly H_2O and CO_2, leads to undesired Na^+ extraction. This reaction forms NaOH or Na_2CO_3 on the material's surface, deteriorating the reversibility and kinetics of the charge/discharge process. Furthermore, when O3-type cathode materials are exposed to water or humid air, the layered structure changes to a Na-less phase, which has a lower capacity than that before exposure [25] To address the moisture instability issues of O3-type cathode materials, a coating capable of preventing direct contact with water or moisture was first suggested. However, this coating strategy requires an additional process, and an inhomogeneous coating layer results in poor ion and electron conductivity. Accordingly, several reports suggested the doping strategy to enhance the moisture stability of O3-type cathode materials. For example, Mu *et al.* suggested that the Cu^{2+}-incorporated structure could avoid oxidation by H_2O, CO_2, and O_2 or form different surface structures and compositions that protect the bulk material.[26] However, detailed analyses of how the surface structure changes upon H_2O, CO_2, and O_2 have not been conducted. Similarly, Yao *et al.* improved the moisture stability of O3-type $NaNi_{0.5}Mn_{0.5}O_2$ using Cu^{2+}/Ti^{4+} co-doping.[27] They found that this co-doping approach reduced the Na^+ layer distance and modulated the electronic structure of the transition metal layer, effectively preventing Na^+ extraction and oxidation of transition metals during moisture exposure. Despite these studies, a comprehensive understanding of the mechanism by which doping suppresses the degradation of materials due to contact with moisture is still lacking.

In this study, we prepared O3-type $NaNi_{0.3}Fe_{0.2}Mn_{0.5}O_2$ (NFM325) and $NaNi_{0.3}Fe_{0.2}Cu_{0.1}Mn_{0.4}O_2$ (NFCM3214) cathode materials *via* a simple sol–gel route. Through comparative analyses of the two materials, Cu doping effects on moisture stability and electrochemical properties were investigated. X-ray diffraction (XRD) analysis reveals that Cu^{2+} doping improves the bulk structure stability against water exposure. To further examine surface degradation induced by water, Fourier-transform infrared (FTIR) spectroscopy, X-ray photoelectron spectroscopy (XPS), and time-of-flight secondary ion mass spectrometry (TOF-SIMS) were employed. The results indicate that Cu doping significantly suppresses the formation of sodium residues on the surface after water exposure. Additionally, transmission electron microscopy (TEM) demonstrated that Cu doping prevents the formation of a hydrated ion mixed phase on the surface, which has a rock salt structure. These findings confirmed that Cu doping effectively suppresses the migration of sodium and transition metal ions within both bulk and surface structures upon water exposure. Furthermore, electrochemical evaluations revealed that Cu doping effectively improves the electrochemical properties by enhancing Na ion diffusion in the structure.

2. Experimental section

2.1. Material preparation

Synthesis of O3-type $NaNi_{0.3}Fe_{0.2}Mn_{0.5}O_2$ (NFM325) and $NaNi_{0.3}Fe_{0.2}Cu_{0.1}Mn_{0.4}O_2$ (NFCM3214). NFM325 was prepared using the sol–gel route. Stoichiometric amounts of nickel(II) acetate tetrahydrate ($Ni(CH_3COO)_2 \cdot 4H_2O$, Sigma-Aldrich, 98%), iron(III) nitrate nonahydrate ($Fe(NO_3)_3 \cdot 9H_2O$, Sigma-Aldrich, 98%), and manganese(II) acetate tetrahydrate ($Mn(CH_3COO)_2 \cdot 4H_2O$, Sigma-Aldrich, 98%) were dissolved in distilled water. Sodium acetate (CH_3COONa, Sigma-Aldrich, 99.7%) and citric acid ($C_6H_8O_7$, Sigma-Aldrich, 99.5%) were added to the aqueous solution. The solution was evaporated with stirring at 80 °C for 6 h, and the gel-like precursor obtained was completely dried at 120 °C for 12 h. The dried gel-like precursor was pre-calcined at 500 °C in air for 5 h. The final cathode material was acquired by the calcination process at 850 °C for 24 h. The same procedure was implemented for obtaining NFCM3214, while copper(II) acetate hydrate ($Cu(II)(CH_3COO)_2 \cdot H_2O$, Sigma-Aldrich, 98%) was added for Cu^{2+} doping.

2.2. Material characterization

The crystal structure was characterized with a powder X-ray diffractometer (D8 Advance, Bruker, US) using Cu Kα radiation with a 0.02° min^{-1} scan rate in a 2θ range of 15–80°. The structural parameters of the powder were determined by the Rietveld refinement method using TOPAS V5 (Bruker, US). Fourier transform infrared (FT-IR) spectra were acquired with an iS10 (Thermo Fisher Scientific, US) spectrometer in the wavenumber range of 400–4000 cm^{-1}. Thermogravimetric analysis (TGA) curves were obtained with the Q600 (TA

Instruments, US) equipment. X-ray photoelectron spectroscopy (XPS) was conducted with a PHI 5000 VersaProbe (ULVAC PHI, Japan) using Al Kα radiation (1487 eV), and deconvolution of all peaks was conducted using the MultiPak (ULVAC PHI, Japan) program. Time-of-flight secondary ion mass spectroscopy (ToF-SIMS) was implemented with a TOF-SIMS.5 instrument (ION-TOF, Germany). The morphology of as-prepared materials was confirmed using field-emission scanning electron microscopy (FE-SEM, Teneo VolumeScope, FEI, US). The microstructure selected-area electron diffraction (SAED) patterns were obtained by high-resolution transmission electron microscopy (HR-TEM). Scanning transmission electron microscopy (STEM) and electron energy loss spectroscopy (EELS) images were obtained in the STEM mode. These TEM analyses were implemented employing a Titan 80-300 (FEI) instrument at 300 keV. Energy dispersive X-ray analysis (EDS) mapping data were acquired through a transmission electron microscope (TEM) on a Talos F200X instrument (FEI, US) at 200 keV with a high-brightness Schottky field-emission electron source (X-FEG, Thermo Fisher Scientific, US) and a Super-X EDS detector system (Bruker, US). The *in situ* X-ray diffraction (*in situ* XRD) measurements were carried out using an R-AXIS IV++ X-ray diffractometer (Rigaku, Japan). The crystal structure and data collection were done using Mo Kα radiation with a wavelength of 0.7107 Å, and the data were recorded on an image plate with an exposure time of 150 s. After collecting the data, the 2θ angles of all the XRD patterns have been converted to Cu Kα radiation with a wavelength of 1.54 Å for easy comparison. To prepare the cells for *in situ* XRD measurements, CR-2032-type coin cells were fabricated separately in a glove box. The cells were cycled using a WBCS3000K8 multichannel cycler (WonA-Tech, Korea) in the voltage range of 2.0–4.3 V.

2.3. Electrochemical measurements

All the electrochemical tests were conducted with a CR-2032 sodium coin-type half cell (Hoshen, Japan). For the electrode preparation, a slurry was made by mixing the active material, conductive material (Super P) and poly(vinylidene fluoride) (PVDF) binder in *N*-methyl-2-pyrrolidone (NMP) solvent with a weight ratio of 8 : 1 : 1. The slurry was pasted with a doctor blade (100 μm) on a piece of Al foil to obtain a loading mass of 8–9 mg cm^{-2}. The NMP solvent was evaporated at 80 °C in a vacuum oven for 24 h. Sodium half cells were assembled with Na foil and glass-fiber separator (GF/F, Whatman, UK). For the electrolyte, 1 M $NaPF_6$ salt was dissolved in a mixed solvent of ethylene carbonate (EC), propylene carbonate (PC), and diethyl carbonate (DEC) (1 : 1 : 1 v/v). Cyclic voltammetry (CV, VSP-300 potentiostat, BioLogic Science Instruments, France) was carried out using EC-Lab software to investigate redox reactions in the potential range of 2.0–4.3 V (*vs.* Na^+/Na) at various scan rates (0.1, 0.2, 0.4, 0.6, 0.8, and 1.0 mV s^{-1}) by. Galvanostatic cycling tests were performed on a MACCOR Series 4000 (Thermotech, US) cycler in the voltage range of 2.0–4.3 V (*vs.* Na^+/Na) at room temperature. All electrochemical tests were conducted after cell activation with 3 pre-cycles at 14 mA g^{-1}. For the full cell configuration, MoS_2 was employed as the anode material with an N/P ratio of 1.2, and 30 μL of electrolyte was used, corresponding to an E/C ratio of ~29 μL mAh^{-1}.

3. Results and discussion

Fig. 1a and b show XRD patterns of the as-prepared NFM325 and NFCM3214 powder samples, respectively. The XRD pattern of NFM325 in Fig. 1a proves that a complete hexagonal α-$NaFeO_2$ structure (space group: $R\bar{3}m$) is synthesized after calcination. The XRD pattern of NFCM3214 (Fig. 1b) also reveals a typical O3-type structure with no evidence of a secondary phase or impurity. For a more comprehensive understanding of crystallographic details, we conducted Rietveld refinement of both samples. The refined crystallographic data are summarized in Table S1. Interestingly, the Na occupancy of NFM325 is 0.791, while that of NFCM3214 is 0.930; hence, we assumed that Na^+ content in NFM325 is partially extracted during the cooling after the calcination process at high temperature (>800 °C), and it causes a Na^+ deficient surface. The previous study has demonstrated that H_2O molecules can intercalate into the Na layer and react with Na^+.[27] The partial extraction of Na^+ ions leads to an expansion of the Na layer, which in turn accelerates the insertion and reaction of H_2O molecules into the O3 phase upon water/moisture air exposure. For the lattice parameters listed in Table S1, the *c* lattice parameter of NFM325 is larger than that of NFCM3214. This result also indicates that Na^+ extraction from the Na layer is impeded by Cu doping during synthesis. Furthermore, *c*-axis contraction can improve the water stability of the O3 phase, as it creates a less favourable environment for the insertion of H_2O molecules into the Na layer. To verify the elemental composition of both samples, inductively coupled plasma (ICP) measurements were performed. The results confirm that the overall transition metal ratios are consistent with the intended compositions for both NFM325 and NFCM3214 (Table S2). Notably, the Na contents of NFM325 and NFCM3214 were found to be nearly identical. This suggests that the Na extracted from the NFM325 structure during synthesis did not result in an overall loss of Na but instead contributed to the formation of residual Na-containing species.

To compare the water stability of NFM325 and NFCM3214, we immersed the powder samples in distilled water (pH 7.0) with stirring for 10 minutes. After soaking, the pH of the resulting solutions was measured. The aqueous solution containing NFM325 exhibited a pH of 13.3, while that of NFCM3214 was 11.8 (Fig. S1), indicating that the pH increase originates from the powder samples themselves. According to previous reports, water molecules can release protons (H^+) that exchange with sodium ions (Na^+) in O3-type $NaTMO_2$ materials, following the hydrolysis reaction: $NaTMO_2 + xH_2O \rightarrow Na_{1-x}H_xTMO_2 + NaOH$.[26,28,29] Based on this mechanism, the observed increase in pH is attributed to NaOH generation, arising from both residual NaOH formed during synthesis and NaOH produced through Na^+/H^+ exchange upon water exposure. These results suggest that Cu^{2+} doping effectively suppresses both the formation of residual sodium species and the hydration-induced degradation of the O3 phase when in contact with water. To further

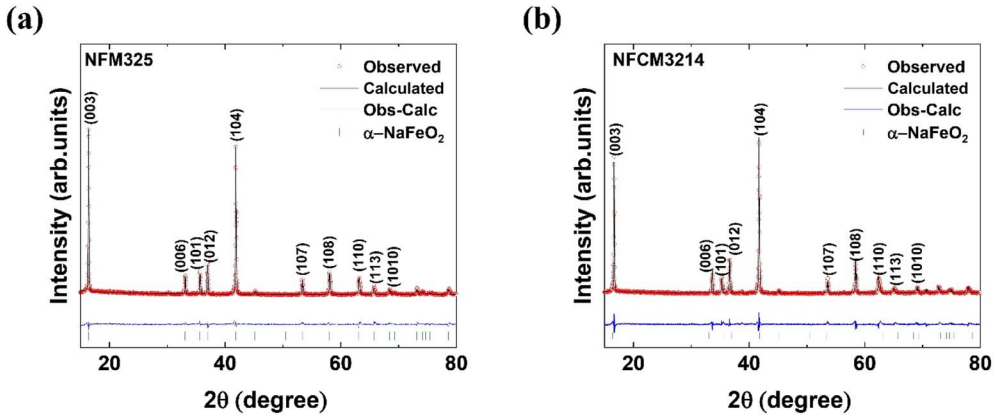

Fig. 1 Results of Rietveld refinement of as-prepared (a) NFM325 and (b) NFCM3214 powders.

verify the extent of Na extraction during the water exposure, ICP analysis was performed on the powder samples after immersion. The Na molar ratio of NFM325 decreased markedly from 0.99 to 0.25, whereas NFCM3214 showed a much smaller change from 1 to 0.61 (Table S3). This result confirms that NFM325 undergoes more severe Na^+ leaching upon water exposure, which is consistent with its higher pH value and enhanced NaOH formation. In contrast, the relatively stable Na content in NFCM3214 further supports the improved water stability induced by Cu^{2+} doping. To quantitively evaluate the total amount of NaOH generated during synthesis and water exposure, acid–base titration was performed on the solutions after immersion (Fig. S2). Based on these results, the amount of NaOH was calculated to be 6.39 mmol g^{-1} for NFM325 and 3.01 mmol g^{-1} for NFCM3214. Notably, the NaOH content in NFCM3214 was reduced by more than 50% compared to NFM325, indicating that Cu^{2+} doping effectively suppresses the formation of residual NaOH. In addition, the amount of Na_2CO_3 was also quantified to be ~0.31 mmol g^{-1} for both samples, which is negligible compared to NaOH, indicating that the overall alkalinity is predominantly governed by NaOH.

The XRD pattern of dried NFM325 (Fig. 2a) reveals clear signs of structural degradation after water exposure. In particular, a broad peak appears at a lower 2θ value (14.38°), which is indicative of the formation of a highly disordered hydrated O3 phase, commonly referred to as the α-$Na_{1-x}FeO_2$ structure, characterized by low sodium content.[24] Furthermore, the (104) reflection—characteristic of the pristine α-$NaFeO_2$ structure—disappears, while the (003) peak shifts to a lower angle. This shift implies an expansion of the *c*-axis lattice parameter, likely due to proton (H^+) or water (H_2O) insertion into the layered structure.[30–32] These results confirm significant structural changes in NFM325 during water soaking. These results confirm that NFM325 undergoes substantial structural disruption upon contact with water. In contrast, the XRD pattern of dried NFCM3214 remains largely unchanged after water exposure, indicating that Cu^{2+} doping effectively suppresses water-induced structural degradation in the O3-type layered oxide framework.

To confirm the formation of NaOH on the particle surface following water exposure, FT-IR analyses were performed on each water-soaked powder sample in the range of 1000–4000 cm^{-1} (Fig. 2b). Prior to soaking, both samples exhibited an absorption peak at ~1450 cm^{-1}, corresponding to Na_2CO_3, with the intensity of this peak being higher in NFM325 than in NFCM3214. This suggests that more sodium carbonate residue is generated during the synthesis of NFM325. After soaking, the Na_2CO_3 peak disappears in both samples, while a new O–H stretching vibration peak emerges at ~3300 cm^{-1}. Notably, the water-soaked NFM325 sample shows a much more intense O–H vibration peak compared to NFCM3214, indicating a greater amount of NaOH formation. These results suggest that Cu^{2+} doping effectively suppresses the generation of NaOH on the surface by inhibiting Na^+ extraction from the sodium layers in the O3 structure. The suppression of Na^+/H^+ exchange during water exposure by Cu^{2+} doping was further supported by thermogravimetric analysis (TGA) conducted under a nitrogen atmosphere (Fig. 2c). Both fresh NFM325 and NFCM3214 powders showed negligible weight loss between 100 and 400 °C. However, the dried NFM325 powder after water soaking exhibited a pronounced two-step weight loss totaling 13.24 wt%. The initial weight loss below 100 °C is attributed to the desorption of physically adsorbed water, while the second step above 100 °C is ascribed to H^+ desorption from the structure.[27,33] In contrast, the dried NFCM3214 powder after water soaking showed no weight loss below 100 °C and only a minor total weight loss of 1.96 wt%, highlighting the superior water stability of the NFCM3214 material.

To elucidate the effect of water contact on the particle surface, X-ray photoelectron spectroscopy (XPS) analysis was performed on the water-soaked powders, as shown in Fig. 3. In Fig. 3a, the O 1s spectra of fresh NFM325 and NFCM3214 were deconvoluted into three peaks corresponding to the Na KLL Auger (534.1 eV), OH^- (530.9 eV), and transition metal–oxygen bonds (Me–O, 529.2 eV).[35] No significant differences were observed between the two materials in their pristine state. After water soaking, both materials exhibited a shift of the Na KLL Auger peak from 534.1 to 535.1 eV, as well as an increase in the OH^- peak intensity (Fig. 3b). These changes indicate that Na^+ extracted *via* Na^+/H^+ exchange generates NaOH on the particle surface during water exposure. Notably, water-soaked NFM325

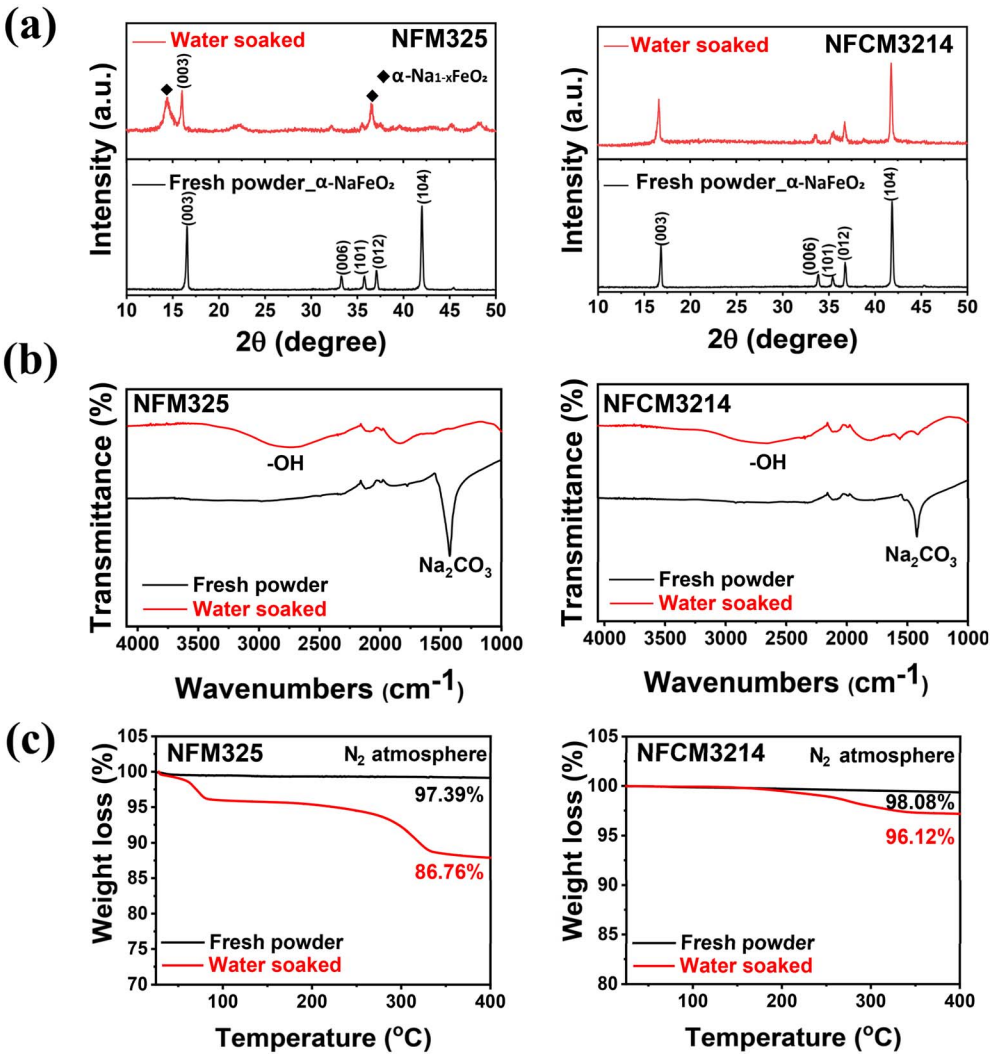

Fig. 2 (a) XRD patterns of fresh and water-soaked NFM325 and NFCM3214 samples. (b) FT-IR spectra of fresh and water-soaked NFM325 and NFCM3214 samples. (c) TGA curves of fresh and water-soaked NFM325 and NFCM3214 samples.

displayed a substantial increase in the OH^- peak, which dominated the O 1s spectrum, reflecting a significant formation of NaOH due to water contact. In contrast, NFCM3214 showed only a minor increase in the OH^- peak intensity after soaking in water. A quantitative comparison of the OH^- and Me–O peak areas further revealed that the OH^- peak area ratio in water-soaked NFCM3214 (64%) was considerably lower than that in NFM325 (90%), indicating less surface NaOH formation in the Cu-doped sample. Consistent with the XPS results, time-of-flight secondary ion mass spectrometry (TOF-SIMS) spectra (Fig. S3) showed that the surfaces of water-soaked NFM325 contained higher amounts of OH^- (O_2H^-), NaOH (NaO_2H^-), and $NaCO_3^-$ species compared to those of NFCM3214.

In Fig. S4, the FE-SEM images of NFM325 and NFCM3214 show no discernible changes in particle morphology or integrity after water exposure, with both samples retaining their characteristic hexagonal shape. Although NaOH-like products may form on the surface following water contact, these products are likely present predominantly at the nanoscale. Notably, the TEM-EDS mapping image of NFM325 after water soaking (Fig. 4a) reveals that, in contrast to other elements such as Na, Ni, Fe, and O, manganese becomes enriched at the particle surface compared to the fresh sample (Fig. S5a). This observation is further supported by EDS line-scanning analysis (Fig. 4b and S5b), which shows an increasing Mn ratio up to approximately 30 nm from the surface, while the fresh NFM325 particles (Fig. S5b) display a nearly uniform elemental distribution, except for a negligible Mn increase at the surface. HR-TEM and fast Fourier transform (FFT) images were obtained to clarify the structure of this Mn-rich surface region. The FFT image (Fig. 4b) indicates the formation of a rock salt-like cubic phase ($Fm\bar{3}m$) following water contact. This suggests that hydrated ion-mixed phases, such as manganese hydroxides or oxides, may form on the surface as the O3-structured layer reacts with water molecules. The surface structure of O3-type layered oxide cathodes is a critical factor for cyclability, as most degradation processes are initiated or accelerated at the interface between the electrolyte and the active material surface, particularly under high-

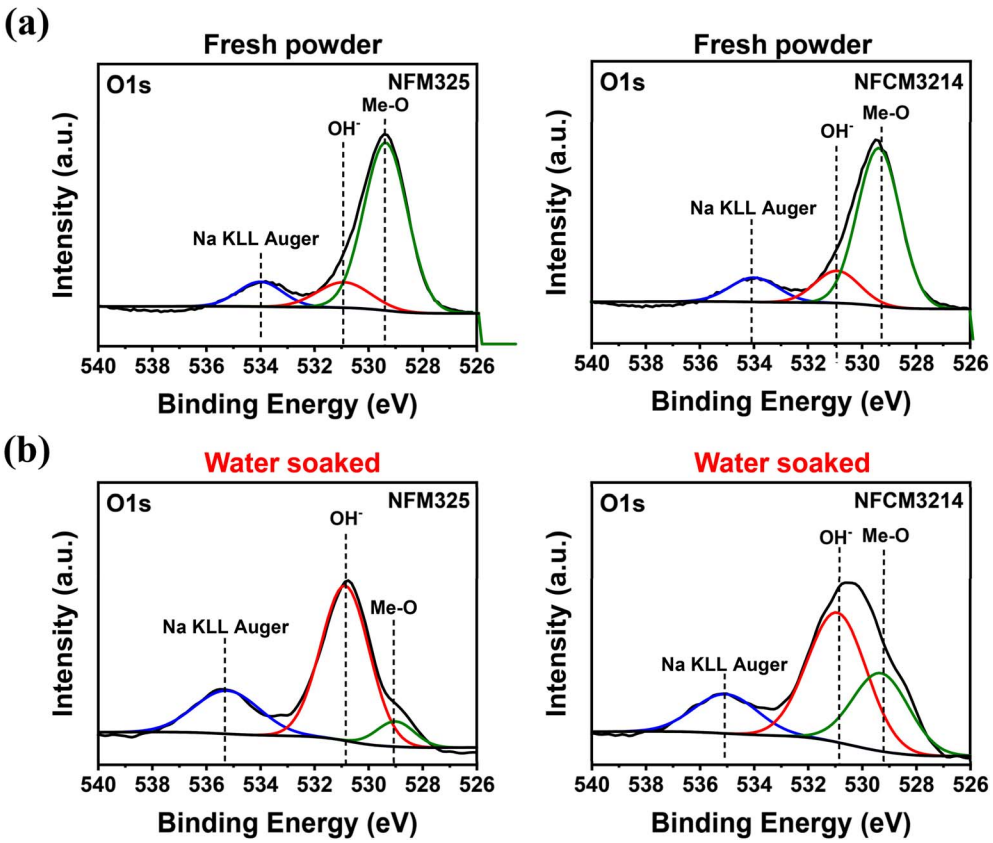

Fig. 3 (a) O 1s XPS spectra of fresh NFM325 and NFCM3214 samples. (b) O 1s XPS spectra of water-soaked NFM325 and NFCM3214 samples.

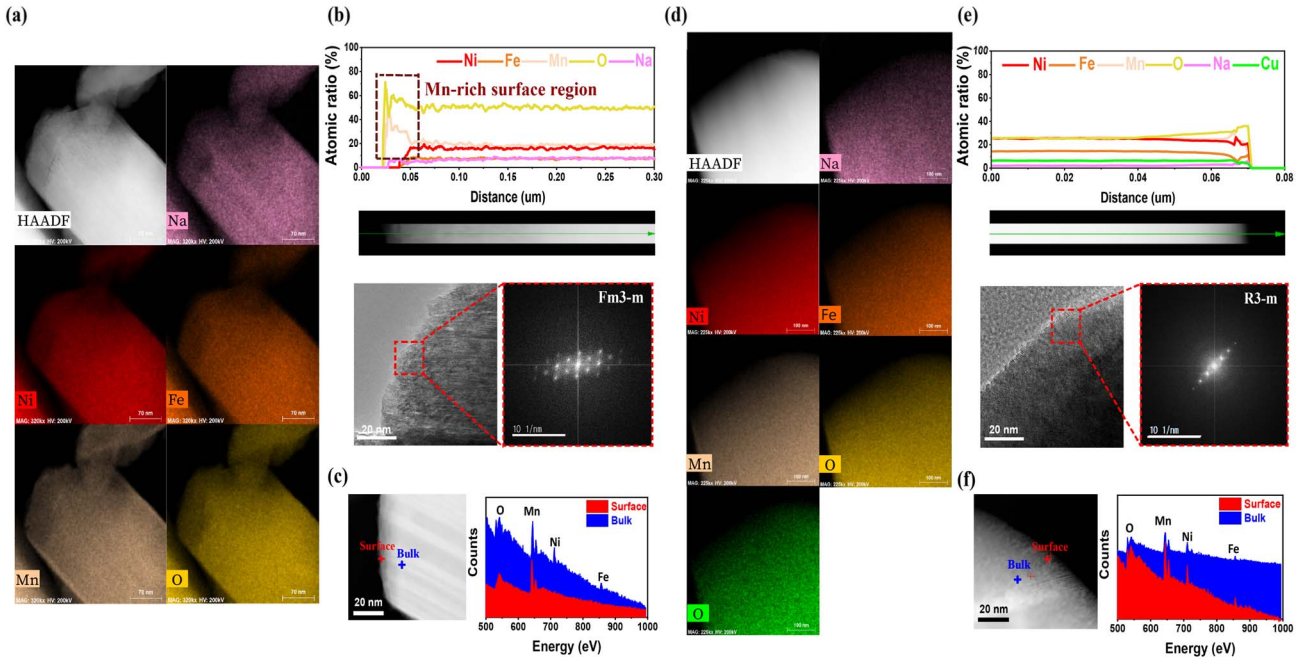

Fig. 4 (a) HAADF TEM and EDS mapping images, (b) EDS line scan, HR-TEM, and FFT images, and (c) STEM image and EELS spectra of the water-soaked NFM325 sample. (d) HAADF TEM and EDS mapping images, (e) EDS line scan, HR-TEM, and FFT images and (f) STEM image and EELS spectra of the water-soaked NFCM3214 sample.

voltage operation. Thus, the formation of a non-ion-conductive hydrated ion-mixed phase at the surface impedes sodium ion conduction, resulting in degraded electrochemical performance. In Fig. 4c, the EELS spectrum of the particle surface after water contact shows only Mn and O peaks, with the Ni and Fe peaks disappearing relative to the bulk. This phenomenon is absent in the EELS spectrum of fresh NFM325 (Fig. S5c), further confirming that manganese hydroxide or oxide forms on the NFM325 surface upon water exposure. In contrast, as shown in Fig. 4d, NFCM3214 exhibits a uniform elemental distribution throughout the particle, with no apparent concentration gradient—consistent with the fresh particle (Fig. S6a). No significant differences in atomic ratios among the elements are observed in fresh NFCM3214 (Fig. S6b). For water-soaked NFCM3214, a constant Mn concentration is detected from the bulk to the surface (Fig. 4e). The EELS spectra of water-soaked NFCM3214 (Fig. 4f) confirm that the surface structure is well preserved, with identical EELS peak intensities for Ni, Fe, Mn, and O at both the surface and in the bulk, consistent with those of the pristine sample (Fig. S6c). These results demonstrate that Cu doping significantly enhances the surface stability of O3-type layered oxides against water-induced degradation.

To evaluate the influence of Cu doping, sodium half-cells were assembled for charge–discharge testing. Fig. 5a and b display cyclic voltammetry (CV) curves recorded at 0.1 mV s^{-1} over the first three cycles, revealing the redox processes of NFM325 and NFCM3214, respectively. The CV traces exhibit two distinct anodic peaks at ~3.04 and ~4.21 V. The lower-voltage peak corresponds to the Ni^{2+}/Ni^{3+} couple, whereas the higher-voltage feature arises from overlapping Ni^{3+}/Ni^{4+}, Fe^{3+}/Fe^{4+}, and anionic O^{2-}/O^{n-} redox processes.[34] For NFM325, cathodic peaks are less pronounced than the corresponding anodic peaks, and a Mn^{4+}/Mn^{3+} peak pair appears below 2.5 V. These observations indicate partial irreversibility and local structural

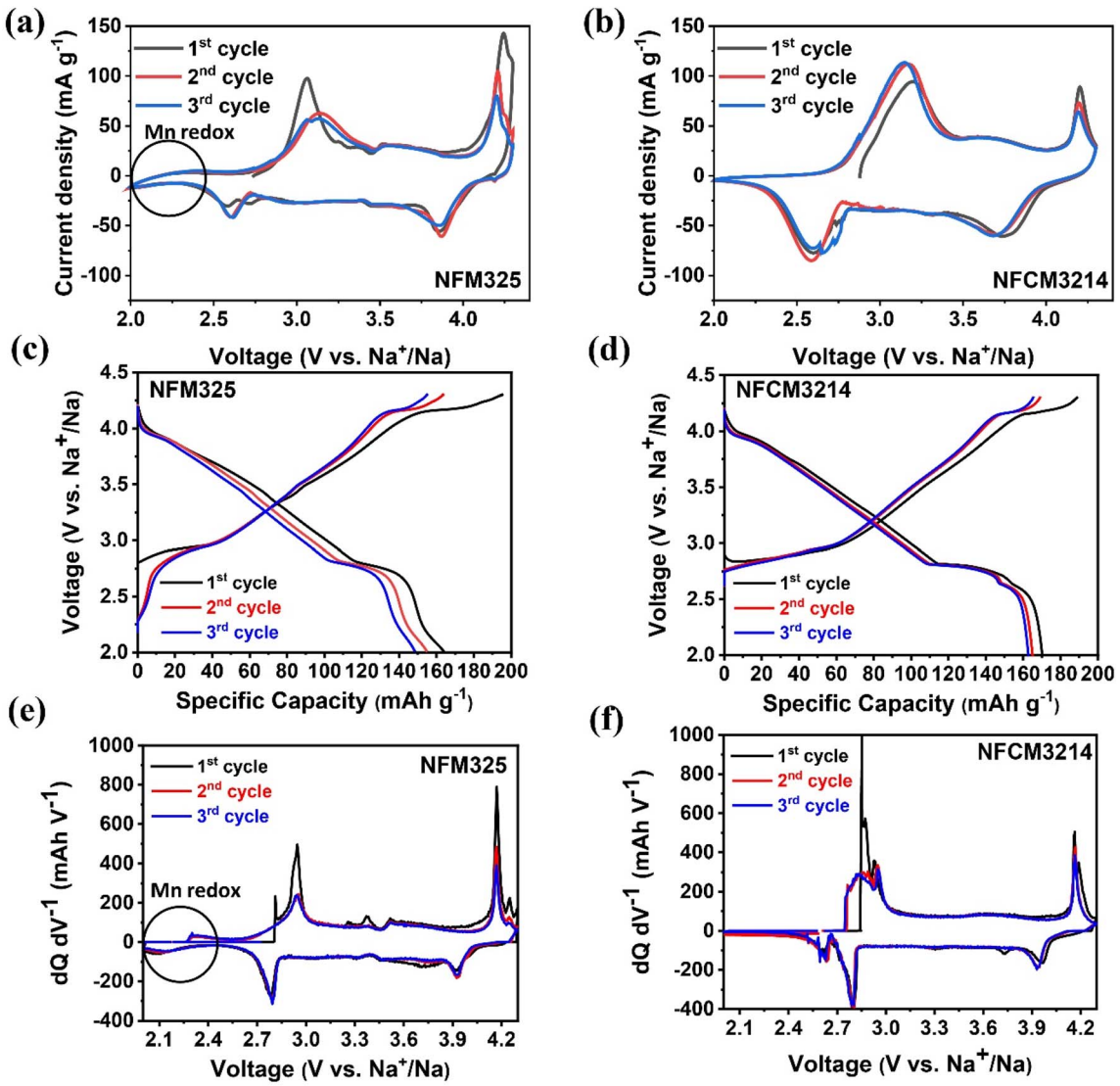

Fig. 5 CV plots at 0.1 mV s^{-1} of the first cycle for (a) NFM325 and (b) NFCM3214 electrodes. Voltage profiles of initial 3 cycles for (c) NFM325 and (d) NFCM3214 in the potential range of 2.0–4.3 V (*vs.* Na^+/Na) at 14 mA g^{-1}. d*Q*/d*V* plots of initial 3 cycles for (e) NFM325 and (f) NFCM3214 in the potential range of 2.0–4.3 V (*vs.* Na^+/Na) at 14 mA g^{-1}.

distortion associated with Jahn–Teller-active Mn^{3+}.[35,36] In contrast, NFCM3214 shows more reversible redox behavior with no discernible Mn-related peaks, implying that Cu doping suppresses the formation of Mn^{3+} and enhances the overall reversibility. Consistent with Yoda *et al.*, this suppression can be attributed to a Cu^{2+}/Mn^{4+} charge-balance effect that inhibits Mn^{3+} formation.[37] These assignments are mirrored in the galvanostatic voltage profiles (Fig. 5c and d). For NFM325 (Fig. 5c), charging after the first cycle begins with a low-potential slope/plateau (2.3–2.8 V), consistent with Mn^{3+} participation. The discharge capacity at 0.1C declines over the first three cycles from 164.3 to 148.7 mAh g^{-1} (164.3, 155.1, and 148.7 mAh g^{-1} for the first to third cycles, respectively). In NFCM3214, the Mn^{3+}-related slope is absent even after the first cycle, and capacity retention is improved: the discharge capacity at 0.1C decreases only slightly from 170.2 to 162.8 mAh g^{-1} (170.2, 165.0, and 162.8 mAh g^{-1} in the first to third cycles). Thus, incorporating electrochemically inactive Cu stabilizes the Mn-based layered cathode and mitigates capacity fade. NFCM3214 also delivers a higher initial coulombic efficiency than NFM325 (90.2% *vs.* 84.2%), indicating greater first-cycle reversibility; the underlying mechanism is discussed in a later section. Differential capacity analysis further supports these trends. In NFM325 (Fig. 5e), the dominant ~4.2 V oxidation peak assigned to Ni^{3+}/Ni^{4+}, Fe^{3+}/Fe^{4+}, and anionic O redox progressively diminishes with cycling, while a distinct Mn^{3+} redox feature grows in.[38] As noted by You *et al.*, Jahn–Teller-active Mn^{3+} can destabilize the local structure during cycling, driving irreversible phase transitions and capacity loss.[39] By contrast, NFCM3214 (Fig. 5f) exhibits only minor attenuation of peak intensity through the third cycle and no Mn^{3+} redox signatures, resulting from Cu^{2+} substitution in the O3-type layered framework suppressing Jahn–Teller-driven local distortions.

Fig. 6a and b present contour maps of the *in situ* XRD patterns collected during the first cycle at 14 mA g^{-1} over 2.0–4.3 V; the corresponding patterns for the first two cycles are provided in Fig. S7a and b. For NFM325 (Fig. 6a), continuous low-angle shifts of the $(003)_{O3}$ and $(006)_{O3}$ peaks are observed within 2.9–3.1 V, accompanied by gradual high-angle shifts of the $(101)_{O3}$ and $(012)_{O3}$ peaks. This evolution is indicative of an O3 → P3 phase transition during charging.[39] Although nearly all peaks of NFM325 return to their original 2θ position corresponding to the O3 phase during the discharge, the $(006)_{O3}$ and $(006)_{P3}$ peaks co-exist after discharging (Fig. S7c). Such O3/P3 coexistence at the start of subsequent cycles reduces the accessible Na^+ inventory—because P3 accommodates less Na than O3—thereby contributing to the capacity decay of NFM325. In contrast, NFCM3214 (Fig. 6b) exhibits a broader, more gradual evolution over the 2.9–3.1 V window, consistent with an extended O3 → P3 transition. Rapid phase transitions can impart interfacial strain and microcracking; the more gradual progression observed for NFCM3214 should alleviate

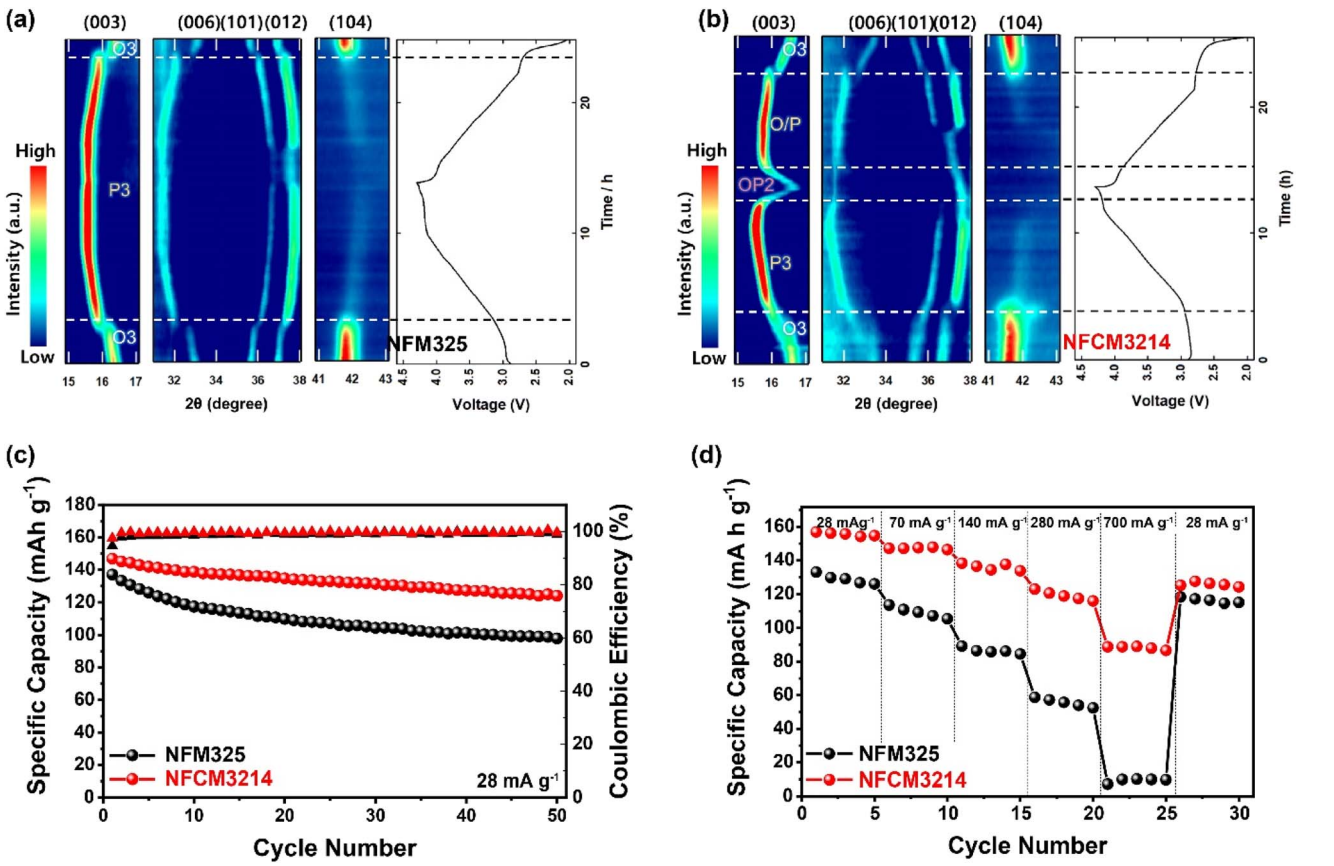

Fig. 6 Intensity contour image for *in situ* XRD patterns of (a) NFM325 and (b) NFCM3214 in the first cycle. (c) Cycling and (d) rate capability tests in the potential range of 2.0–4.3 V (*vs.* Na^+/Na) at 28 mA g^{-1} and various current densities (28, 70, 140, 280, and 700 mA g^{-1}).

such strain and reduce the risk of particle/electrode degradation. Notably, near the end of charging (~4.3 V), the $(003)_{P3}$ and $(006)_{P3}$ peaks shift to higher 2θ values, a behavior previously attributed to a P3 → OP2 restacking transition.[40] The OP2 phase—characterized by alternating octahedral–prismatic oxygen stacking—emerges under Fe^{4+} formation and very low Na content. We speculate that Cu doping facilitates Na^+ transport within the interslab region, enabling deeper desodiation and promoting OP2 formation, which contribute additional high-voltage capacity. This mechanism is consistent with the higher capacity observed for NFCM3214 relative to NFM325. Despite the occurrence of complex phase transitions, which are generally irreversible, all XRD peaks of NFCM3214 return to their original 2θ position after the second cycle (Fig. S7d). This reversibility can be attributed to: (i) facile Na^+ diffusion that supports reversible stacking changes; (ii) the absence of Jahn–Teller-active Mn^{3+} in the electrochemical window, which stabilizes the local structure; and (iii) faster OP2 → O3 restacking relative to P3 → O3, consistent with a smaller change in the *c* lattice parameter.[40] Consequently, Cu doping renders the O3–P3–OP2 transitions more reversible and contributes to the improved capacity and cycling stability of NFCM3214.

Electrochemical data corroborate these structural findings. As shown in Fig. 6c, NFCM3214 exhibits superior capacity retention (84.5%) compared with NFM325 (71.4%). Rate-capability tests (Fig. 6d) further show that NFCM3214 delivers 156.9, 147.2, 138.4, 122.9, and 88.8 mAh g^{-1} at 28, 70, 140, 280, and 700 mA g^{-1}, respectively, whereas NFM325 provides 133.0, 113.5, 89.2, 58.8, and 7.2 mAh g^{-1} at the same *C*-rates. Upon returning to 28 mA g^{-1}, the discharge capacity recovers to 125.2 mAh g^{-1} for NFCM3214 but only to 118.3 mAh g^{-1} for NFM325. Taken together, the Cu^{2+}-doped NFCM3214 displays higher discharge capacities across all current densities and better capacity recovery, consistent with enhanced Na^+-transport kinetics and reduced polarization. To quantify the impact of Cu^{2+} doping on Na^+ transport, cyclic voltammetry (CV) was performed at scan rates of 0.1, 0.2, 0.4, 0.6, 0.8, and 1.0 mV s^{-1} (Fig. S8a and b). Apparent Na^+ diffusion coefficients (D) were extracted from the Randles–Sevcik relation (eqn (1)):

$$I_p = 0.4463nFAC(nFDvRT)^{1/2} \quad (1)$$

where I_p is the peak current, n is the number of electrons, F is the Faraday constant, A is the electrode area, C is the Na^+ concentration in the cathode (mol cm^{-3}), D is the diffusion coefficient (cm^2 s^{-1}), v is the scan rate (V s^{-1}), R is the gas constant, and T is the absolute temperature. In this calculation, n was assumed 1 for the Na^+/Na redox process. The geometric electrode area (A) was 1.13 cm^2. Based on calculated densities and Na stoichiometry, the Na^+ concentration in the cathode was estimated to be 4.09×10^{-2} mol cm^{-3} for NFM325 and 4.06×10^{-2} mol cm^{-3} for NFM3214. The temperature was fixed at 298 K. The constants used were $F = 964\,585$C and $R = 8.314$ J mol^{-1} K^{-1}. The linear dependence of I_p on $v^{1/2}$ enables the determination of D.[41] For NFM325, the calculated D values were 1.284×10^{-9} cm^2 s^{-1} (anodic) and 7.056×10^{-10} cm^2 s^{-1} (cathodic). By contrast, NFCM3214 exhibited markedly higher values of 5.346×10^{-9} cm^2 s^{-1} (anodic) and 1.121×10^{-8} cm^2 s^{-1} (cathodic), corresponding to approximately four-fold (anodic) and sixteen-fold (cathodic) increases relative to NFM325. These results align with the superior rate performance of NFCM3214 and indicate that Cu^{2+} doping substantially accelerates solid-state Na^+ diffusion within the electrode.

To assess electrochemical performance after water exposure, we assembled Na half-cells using water-soaked cathodes. Fig. 7a shows the voltage profiles of water-soaked NFM325 over the first three cycles, revealing a severely reduced first-charge capacity of 72.4 mAh g^{-1}. This loss is attributed to Na^+/H^+ exchange during soaking, which generates surface NaOH and a Na-deficient cathode phase, as discussed previously. In addition, surface Mn hydroxide/oxide layers—confirmed by TEM (Fig. 4)—further deteriorate performance, consistent with the disappearance of the characteristic voltage plateau (Fig. 7a). Correspondingly, the discharge capacities over the first three cycles decrease to 105.0, 94.8, and 90.4 mAh g^{-1}, respectively. By contrast, Fig. 7b shows that water-soaked NFCM3214 delivers a first-cycle charge capacity of 151.7 mAh g^{-1}, indicating that Na^+/H^+ exchange and Mn-hydroxide formation are minimal upon water contact. Its discharge capacities are well preserved—145.0, 136.0, and 135.5 mAh g^{-1} in the first, second, and third cycles, respectively. The cycling data in Fig. 7c further highlight this contrast: after 50 cycles, NFCM3214 retains 99.28 mAh g^{-1} with a coulombic efficiency of 99.64%, whereas NFM325 averages only ~40 mAh g^{-1}, delivering 57.59 mAh g^{-1} and 96.25% coulombic efficiency at the 50th cycle. A similar trend appears in the rate-capability test (Fig. 7d): NFM325 exhibits near-zero discharge capacity at 700 mA g^{-1}, while NFCM3214 maintains substantial capacity across all tested rates. Collectively, these results indicate that Cu^{2+}-doped NFCM3214 is considerably more tolerant to water exposure than NFM325. To further assess moisture stability under conditions relevant to practical storage and handling, the powders were stored at 70 °C and 80% relative humidity for 7 and 14 days, followed by half-cell testing (Fig. S9). While both samples show little difference after 7 days of exposure, a clear divergence emerges after 14 days, as illustrated in Fig. S9. NFM325 exhibits progressively more severe discharge capacity degradation with increasing exposure time, decreasing from 160 to 103 mAh g^{-1} (64% retention after 14 days of exposure). In contrast, NFCM3214 shows a smaller decrease, from 174 to 131 mAh g^{-1} (75% retention after 14 days of exposure) under the same conditions, demonstrating the enhanced moisture stability enabled by Cu^{2+} doping.

To examine practical applicability, we further performed full-cell tests. MoS_2 was selected as a high-capacity anode (~700 mAh g^{-1} for SIBs). An N-doped MoS_2 composite was synthesized following a reported procedure.[42] In Na half-cells (Fig. S9), this anode delivered initial charge/discharge capacities of 745/649 mAh g^{-1} at 67 mA g^{-1}, nearly double that of typical hard carbon anodes (~350 mAh g^{-1}),[43,44] suggesting a high potential energy density for the full cell. Subsequently, an NFCM3214||MoS_2 full cell yielded initial charge/discharge capacities of 128.8/123.1 mAh g^{-1} over 1.0–4.0 V *vs.* Na^+/Na at 14 mA g^{-1} (Fig. 7e), corresponding to a discharge energy density

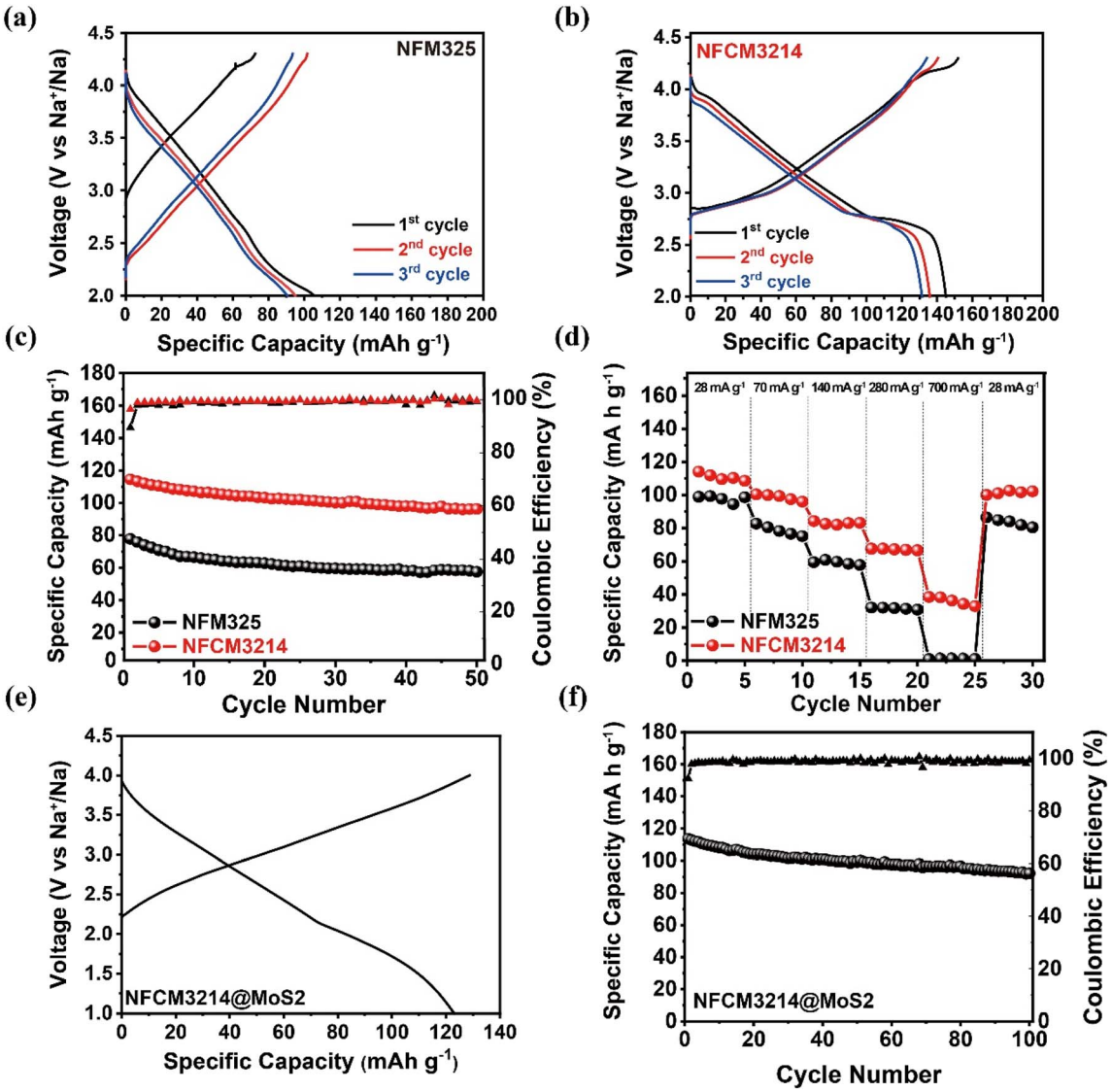

Fig. 7 Voltage profiles of initial 3 cycles for (a) NFM325 and (b) NFCM3214 after water soaking in the potential range of 2.0–4.3 V (*vs.* Na^+/Na) at 14 mA g^{-1}. (c) Cycling and (d) rate capability tests after water soaking in the potential range of 2.0–4.3 V (*vs.* Na^+/Na) at 28 mA g^{-1} and various current densities (28, 70, 140, 280, and 700 mA g^{-1}). (e) Initial voltage profile and (f) cycling of the NFCM3214@MoS_2 cell in the potential range of 1.0–4.0 V (*vs.* Na^+/Na) at 28 mA g^{-1}.

of 315 Wh kg^{-1}. The cell exhibited moderate cycling stability, retaining 81.2% of its capacity over 100 cycles at 28 mA g^{-1} (Fig. 7f), with a gradual capacity decay trend that is likely to persist upon further cycling. These findings underscore the practical promise of NFCM3214 as a cathode for sodium-ion batteries, including under moisture-exposed conditions.

4. Conclusion

Ni/Fe/Mn-based O3-type cathode materials (NFM325 and NFCM3214) were synthesized to elucidate the role of Cu doping in moisture stability and electrochemical performance. Cu incorporation effectively suppressed bulk structural degradation and surface reactions (*e.g.*, NaOH and Mn hydroxide formation) upon water exposure, thereby preserving the electrochemical activity. Electrochemical evaluations of water-soaked electrodes highlight the critical importance of maintaining both bulk and surface integrity for stable operation. Beyond moisture stability, Cu doping substantially enhanced rate capability (improving discharge capacity from 7.2 to 88.8 mAh g^{-1} at 700 mA g^{-1}) and cycling retention (from 71.4% to 84.5% after 100 cycles). Comparative analyses with undoped $NaNi_{0.3}Fe_{0.2}Mn_{0.5}O_2$ reveal that Cu facilitates Na^+ diffusion, mitigates Jahn–Teller distortion, stabilizes intermediate OP2 phases upon deep desodiation, and enables reversible OP2–O/P transitions during cycling. Furthermore, full-cell tests employing NFCM3214 with an N-doped MoS_2 anode confirm its practical feasibility, demonstrating both high capacity and robust cycling stability.

Overall, Cu doping provides an effective strategy to simultaneously enhance structural robustness, ion transport, and

cycling durability of O3-type layered cathodes, underscoring their promise for the practical deployment of sodium-ion batteries.

Author contributions

S. H. Gong conceived the study, designed the methodology, performed the investigation, curated the data, conducted formal analysis, and prepared the original draft and visualizations. H. Kim contributed to methodology design, validation, and investigation. M. K. Cho and S.-C. Kim conducted formal analysis and validation. H. Lim, H. B. Kang, J.-H. Park, and E. Barruna performed the investigation. K. Y. Chung provided resources. W. Chang contributed to validation and manuscript review and editing. W. Choi supervised the study and participated in manuscript review and editing. H.-S. Kim supervised the project, managed project administration, contributed to manuscript review and editing, and secured funding.

Conflicts of interest

There are no conflicts to declare.

Data availability

All data supporting the findings of this study are either included in the article and supporting information (SI) or are available from the corresponding author(s) upon reasonable request.

Supplementary information is available. See DOI: https://doi.org/10.1039/d5ta10289h.

Acknowledgements

This work was supported by National Research Foundation of Korea (NRF) grants and the National Research Council of Science and Technology (NST) grant funded by the Korean Government (MSIT) (No. RS-2024-00407015, RS-2024-00427700 and GTL24011-000).

References

1 T. Liu, Y. Zhang, Z. Jiang, X. Jiang, Z. Jiang, X. Zeng, J. Ji, Z. Li, X. Gao, M. Sun, Z. Lin, M. Ling, J. Zheng and C. Liang, *Energy Environ. Sci.*, 2019, **12**, 1512–1533, DOI: 10.1039/C8EE03727B.

2 J.-H. Hwang, S.-T. Myung and Y.-K. Sun, *Chem. Soc. Rev.*, 2017, **46**, 3529–3614, DOI: 10.1039/C6CS00776G.

3 P. Vassilaras, X. Ma, X. Li and G. Ceder, *J. Electrochem. Soc.*, 2012, **160**, 207–211, DOI: 10.1149/2.023302jes.

4 Y. Nanba, T. Iwao, B. M. Boisse, W. Zhao, E. Honso, D. Asakura, H. Niwa, H. Kiuchi, J. Miyawaki, T. Harada, M. Okubo and A. Yamada, *Chem. Mater.*, 2016, **28**, 1058–1065, DOI: 10.1021/acs.chemmater.5b04289.

5 J.-P. Parent, R. Olazcuaga, M. Devalette, C. Fouassier and P. Hamgenmuller, *J. Solid State Chem.*, 1971, **3**, 1–11, DOI: 10.1016/0022-4596(71)90001-6.

6 C. Delmas, J.-J. Braconnier, C. Fouassier and P. Hagenmuller, *Solid State Ionics*, 1981, **3**, 165–169, DOI: 10.1016/0167-2738(81)90076-X.

7 M. Canini, D. Callegari, M. Bianchini and E. Quartarone, *J. Mater. Chem. A*, 2025, **13**, 31221–31235, DOI: 10.1039/D5TA04988A.

8 S. Komaba, N. Yabuuchi, T. Nakayama, A. Ogata, T. Ishikawa and I. Nakai, *Inorgan. Chem.*, 2012, **51**, 6211–6220, DOI: 10.1021/ic300357d.

9 C. Didier, M. Guignard, C. Denage, O. Szajwaj, S. Ito, I. Saadoune, J. Darriet and C. Delmas, *Electrochem. Solid-State Lett.*, 2011, **14**, 75, DOI: 10.1149/1.3555102.

10 R. Kanno, T. Shirane, Y. Inaba and Y. Kawamoto, *J. Power Sources*, 1997, **68**, 145–152, DOI: 10.1016/S0378-7753(96)02625-0.

11 T. Zhang, Y. Li, Z. Song, Y. Huang, F. Li, S. Cheng and F. Li, *J. Energy Chem.*, 2025, **103**, 294–315, DOI: 10.1016/j.jechem.2024.11.068.

12 N. Yabuuchi, K. Kubota, M. Dahbi and S. Komaba, *Chem. Rev.*, 2014, **114**, 11636–11682, DOI: 10.1021/cr500192f.

13 I. Saadoune, A. Maazaz, M. Menetrier and C. Delmas, *J. Solid State Chem.*, 1996, **122**, 117, DOI: 10.1006/jssc.1996.0090.

14 Y. Xie, G.-L. Xu, H. Che, H. Wang, K. Yang, X. Yang, F. Guo, Y. Ren, Z. Chen, K. Amine and Z.-F. Ma, *Chem. Mater.*, 2018, **30**, 4909–4918, DOI: 10.1021/acs.chemmater.8b00047.

15 J.-Y. Hwang, C. Yoon, I. Belharouak and Y.-K. Sun, *J. Mater. Chem. A*, 2016, **4**, 17952–17959, DOI: 10.1039/C6TA07392A.

16 K. Kubota, N. Yabuuchi, H. Yoshida, M. Dahbi and S. Komaba, *MRS Bull.*, 2014, **39**, 416–422, DOI: 10.1557/mrs.2014.85.

17 N. Yabuuchi, M. Yano, H. Yoshida, S. Kuze and S. Komaba, *J. Electrochem. Soc.*, 2013, **160**, 3131, DOI: 10.1149/2.018305jes.

18 T. Yuan, P. Li, Y. Sun, H. Che, Q. Zheng, Y. Zhang, S. Huang, J. Qiu, Y. Pang, J. Yang, Z.-F. Ma and S. Zheng, *Adv. Funct. Mater.*, 2025, **35**, 2414627, DOI: 10.1002/adfm.202414627.

19 T. Yuan, S. Li, Y. Sun, J.-H. Wang, A.-J. Chen, Q. Zheng, Y. Zhang, L. Chen, G. Nam, H. Che, J. Yang and S. Zheng, *ACS Nano*, 2022, **16**, 18058–18070, DOI: 10.1021/acsnano.2c04702.

20 K.-N. Jung, J.-Y. Choi, H.-S. Shin, H. Huu, W. Im and J.-W. Lee, *Solid State Sci.*, 2020, **106**, 106334, DOI: 10.1016/j.solidstatesciences.2020.106334.

21 X. Sun, Y. Jin, C.-Y. Zhang, J.-W. Wen, Y. Shao, Y. Zang and C.-H. Chen, *J. Mater. Chem. A*, 2014, **2**, 17268–17271, DOI: 10.1039/C4TA03828B.

22 M. Leng, J. Bi, W. Wang, Z. Xing, W. Yan, X. Gao, J. Wang and R. Liu, *J. Alloys Compd.*, 2020, **816**, 152581, DOI: 10.1016/j.jallcom.2019.152581.

23 W. Qin, Y. Liu, J. Liu, Z. Yang and Q. Liu, *Electrochim. Acta*, 2022, **418**, 140357, DOI: 10.1016/j.electacta.2022.140357.

24 S. Han, H. Lim, J. Jeong, D. Ahn, W. Park, K.-S. Sohn and M. Pyo, *J. Power Sources*, 2015, **277**, 9–16, DOI: 10.1016/j.jpowsour.2014.11.150.

25 E. Monyoncho and R. Bissessur, *Mater. Res. Bull.*, 2013, **48**, 2678–2686, DOI: 10.1016/j.materresbull.2013.03.027.

26 L. Mu, S. Xu, Y.-S. Hu, H. Li, L. Chen and X. Huang, *Adv. Mater.*, 2015, **27**, 6928–6933, DOI: 10.1002/adma.201502449.

27 H.-R. Yao, P.-F. Wang, Y. Gong, J. Zhang, X. Yu, L. Gu, C. Ouyang, Y.-X. Yin, E. Hu, X.-Q. Yang, E. Stavitski, Y.-G. Guo and L.-J. Wan, *J. Am. Chem. Soc.*, 2017, **139**, 8440–8443, DOI: 10.1021/jacs.7b05176.
28 W. Zuo, J. Qiu, X. Liu, F. Ren, H. Liu, H. He, C. Luo, J. Li, G. Ortiz, H. Duan, J. Liu, M.-S. Wang, Y. Li, R. Fu and Y. Yang, *Nat. Commun.*, 2020, **11**, 3544, DOI: 10.1038/s41467-020-17290-6.
29 F. Ding, Q. Meng, P. Yu, H. Wang, Y. Niu, Y. Li, Y. Yang, X. Rong, X. Liu, Y. Lu, L. Chen and Y.-S. Hu, *Adv. Funct. Mater.*, 2021, **31**, 2101475, DOI: 10.1002/adfm.202101475.
30 Y. You, A. Dolocan, W. Li and A. Manthiram, *Nano Lett.*, 2018, **19**, 182–188, DOI: 10.1021/acs.nanolett.8b03637.
31 Y.-M. Zheng, X.-B. Huang, X.-M. Meng, S.-D. Xu, L. Chen, S.-B. Liu and D. Zhang, *ACS Appl. Mater. Interfaces*, 2021, **13**, 45528–45537, DOI: 10.1021/acsami.1c12684.
32 S. Ching, D. Petrovay, M. Jorgensen and S. Suib, *Inorg. Chem.*, 1997, **36**, 883–890, DOI: 10.1021/ic961088d.
33 Z. Lu and J. Dahn, *Chem. Mater.*, 2001, **13**, 1252–1257, DOI: 10.1021/cm000721x.
34 Y. Zhang, M. Wu, W. Teng, J. Ma, R. Zhang and Y. Huang, *ACS Appl. Mater. Interfaces*, 2020, **12**, 15220–15227, DOI: 10.1021/acsami.0c00386.
35 P. Zhou, Z. Che, F. Ma, J. Zhang, J. Weng, X. Wu, Z. Miao, H. Lin, J. Zhou and S. Zhuo, *Chem. Eng. J.*, 2021, **420**, 127667, DOI: 10.1016/j.cej.2020.127667.
36 W. Xiong, Z. Liu, W. Cheng, J. Zheng, Y. Zou, X. Chen and Y. Liu, *J. Energy Chem.*, 2025, **103**, 59–67, DOI: 10.1016/j.jechem.2024.10.058.
37 Y. Yoda, K. Kubota, K. Kuroki, S. Suzuki, K. Yamanaka, T. Yaji, S. Amagasa, Y. Yamada, T. Ohta and S. Komaba, *Small*, 2020, **16**, 2006483, DOI: 10.1002/smll.202006483.
38 J. Xu, J. Chen, K. Zhang, N. Li, L. Tao and C.-P. Wong, *Nano Energy*, 2020, **78**, 105142, DOI: 10.1016/j.nanoen.2020.105142.
39 Y. You and A. Manthiram, *Adv. Energy Mater.*, 2018, **8**, 1701785, DOI: 10.1002/aenm.201701785.
40 J. Kim, D.-H. Kwon, J. Yang, H. Kim, S.-H. Bo, L. Wu, H. Kim, D.-H. Seo, T. Shi, J. Wang, Y. Zhu and G. Ceder, *Adv. Energy Mater.*, 2020, **10**, 201151, DOI: 10.1002/aenm.202001151.
41 X.-H. Rui, N. Ding, J. Liu and C. Chen, *Electrochim. Acta*, 2010, **55**, 2384–2390, DOI: 10.1016/j.electacta.2009.11.096.
42 H. Lim, H. Kim, S.-O. Kim and W. Choi, *Chem. Eng. J.*, 2020, **387**, 124144, DOI: 10.1016/j.cej.2020.124144.
43 M. Song, Z. Yi, R. Xu, J. Chen, J. Cheng, Z. Wang, Q. Liu, Q. Guo, L. Xie and C. Chen, *Energy Storage Mater.*, 2022, **51**, 620–629, DOI: 10.1016/j.ensm.2022.07.005.
44 P. Bai, Y. He, X. Zou, X. Zhao, P. Xiong and Y. Xu, *Adv. Energy Mater.*, 2018, **8**, 1703217, DOI: 10.1002/aenm.201703217.

